

MEDS-Net: Self-Distilled Multi-Encoders Network with Bi-Direction Maximum Intensity projections for Lung Nodule Detection

Muhammad Usman^{1,2}, Azka Rehman¹, Abdullah Shahid¹, Siddique Latif³, Shi-Sub Byon¹, Byoung-Dai Lee^{4,*}, Sung-Hyun Kim¹, Byung-il Lee¹, and Yeong-Gil Shin²

¹Center for Artificial Intelligence in Medicine and Imaging, HealthHub Co. Ltd., Seoul, 06524, South Korea

²Department of Computer Science and Engineering, Seoul National University, Seoul, 08826, Republic of Korea

³University of Southern Queensland, Springfield, Queensland 4300, Australia

⁴School of Computer Science and Engineering, Kyonggi University, Suwon, 16227, South Korea

Abstract—Early detection of lung cancer is an effective way to improve the survival rate of patients. It is a critical step to have accurate detection of lung nodules in computed tomography (CT) images for the diagnosis of lung cancer. However, due to the heterogeneity of the lung nodules and the complexity of the surrounding environment, it is a challenge to develop a robust nodule detection method. Numerous efforts have been made to develop an efficient Computer-aided detection (CADe) systems, albeit none compliance with the routine workflow of radiologists which limits the adaptability of such CADe system. To overcome this deficiency, in this study we propose a lung nodule detection scheme which fully incorporates the clinic workflow of radiologists. Particularly, we exploit Bi-Directional Maximum intensity projection (MIP) images of various thicknesses (i.e., 3, 5 and 10mm) along with 3D patch of CT scan, consisting of 10 adjacent slices to feed into self distillation based Multi-Encoders Network (MEDS-Net). The propose architecture first condense 3D patch input to three channels by using dense block which consists of dense units which effectively examines the nodule presence from 2D axial slices. This condensed information, along with the forward and backward MIP images is fed to three different encoders to learn the most meaningful representation which is forwarded into decoded block at various levels. At decoder block, we employ self distillation mechanism by connecting the distillation block which contains five lung nodule detectors. It helps to expedite the convergence and improves the learning ability of proposed architecture. Finally, the propose scheme reduces the false positives by complementing the main detector with auxiliary detectors. The proposed scheme has been rigorously evaluated on 888 scans of LUNA16 dataset and obtained a CPM score of 93.6%. The results demonstrate that incorporating of bi-direction MIP images enables MEDS-Net to effectively distinguish nodules from surroundings which helps to achieve the sensitivity of . false positives per scans with the sensitivity of 91.5% and 92.8% with the false positive rate of 0.25 and 0.5 per scan, respectively.

I. INTRODUCTION

Lung cancer has the highest incidence and mortality rates worldwide [1]. Early diagnosis and treatment of pulmonary nodules can increase the survival rate of patients. Computed tomography (CT) has been widely used and proved effective for detecting pulmonary nodules. Accurate and precise nodule segmentation can provide more in-depth assessment of the shape, size and change rate of the nodule. When nodule is

identified, a follow up scan in 3 - 12 months is usually required to assess its growth rate [2]. The growth of the lung tumor may be an indicator for malignancy, and an accurate nodule segmentation can be used for measuring the growth rate of the nodule. However, manually identifying nodules in CT scans is often time-consuming and tedious, because a radiologist needs to read the CT scans slice by slice, and depending upon the slice thickness, a chest CT may contain over 500 slices. Meanwhile, it is also error-prone for the radiologist to detect lots of nodules because of fatigue. To alleviate this problem, computer-aided detection (CAD) plays an increasingly important role to assist radiologists in staging lung cancer tumors. It also helps to improve the accuracy of lung nodule detection as well as to reduce the number of missed nodules [3].

Owing to the advancements in the industrial applications for lung cancer detection and diagnosis, the lung cancer death rate is comparatively reduced. Various commercially available Computer Aided Detection (CADe) systems have shown potential to improve the accuracy of the detection and the diagnosis process [4]. However, due to the heterogeneity of lung nodules and high degree of similarity between the lung nodules and their surrounding tissues, developing a highly accurate and robust CADe system is still a challenging problem. Subsequently, numerous efforts have been made to develop a highly accurate, robust and well-performing pulmonary CADe system [5]–[7]. In general, these diverse nodule detection techniques are divided into two categories: traditional methods and deep learning (DL) based methods. The traditional methods, mainly consisting of classical image processing methods and machine learning classifiers, determine nodules and eliminate FPs by maximizing the matching rate between the feature profiles and suspicious area under the premise of manual-defined specific features. The traditional lung nodule detection approaches utilize morphological operations, threshold-based methods, clustering algorithms, and energy optimization algorithms [8], [9]. Such algorithms consist of long complex pipelines to accomplish the nodule detection tasks. These pipelines use a variety of algorithms to detect the lung region,

select candidate objects, extract discriminating features, and perform the final false positive reduction and classification [10]–[12]. A great deal of expertise and time is needed to design and implement each of these steps, and then to fine-tune the hyper-parameters that control the performance of each sub-component. Most importantly, these methods have limitations in term of overall nodule detection performance and lack the robustness to variation of CT scans.

Recently, DL-based techniques have made vast inroads into in various industrial applications due to their commendable performance [13], e.g., for objects classification [14], counting [15], for quality inspection [16] and recognition [17]. Similarly, DL-based techniques have been extensively proposed for lung nodule detection in practical scenarios [7] [18]–[21]. Mostly DL-based CADe systems consist of two stages: screening and false positive reduction. Former one is typically applied to identify suspicious candidate locations in a patient’s exam. The latter stage is to reduce the FPs by applying the additional DNNs. For instance, Cao et al. [22], proposed two stage CADe system which consists of an improved U-Net architecture for candidate deduction. They divided the scan region into three categories based on the distance from nodule and its intensity value. They used two phase inference scheme, i.e., first rough segmentation and then perform the fine segmentation in the smaller local region. To eliminate the false positives 3D-CNN based ensemble learning architecture was employed. Similarly, Pexeshk et al., [23] applied 3D-CNN for initial screening of lung nodules and FPs are reduced an ensemble of 3-D CNNs trained using extensive transformations applied to both the positive and negative patches to augment the training set. Zhao et al. [24] employed the high-resolution fused attention module, containing the channel and spatial attentions the global information and spatial information of focal nodules. For FPs reduction by scratching the discriminative features of lung nodules by using an adaptive Res-class 3D-CNN framework which is inputted Volume of interest (VOIs) with three different dimensions to encode multilevel contextual information. In [25], Xie et. al. used 2D CNN by incorporating the structure of Faster R-CNN with two region proposal networks and a deconvolutional layer to detect nodule candidates. At second stage, a boosting architecture based on 2D CNN is employed for false positive reduction. [26] employed the classical 2D-based Yolov5 model to locate the nodules roughly on axial slices for nodule detection. The second aggregation stage proposes a candidate nodule selection (CNS) algorithm to locate further and reduce redundant candidate nodules. In [27], Yuan et. al. presented dual stage scheme which utilized 3-D Residual U-Net with channel attention and applied multi-task learning with multi-branch classifier network for nodule detection and false positives reduction, respectively. Similarly in [28] used Mask Region-Mask Region-Convolutional Neural Network (Mask R-CNN) to detect bounding boxes in axial slices and used a classifier ensemble based on CT attenuation patterns to boost 3D pulmonary nodule classification performance. In [29] 3D region proposal network to generate pulmonary nodule candidates and the multi-scale feature maps are used to reduce the false positives. These dual-stage methods increases the

computational cost of the overall solution and a major problem of such CADe systems is that misdiagnosis and omission in the preceding stages greatly impact the subsequent stages. All the nodules that are missed at first stage, i.e., candidate detection stage, will not be recovered later, therefore needs to have very high sensitivity which comes at the cost of producing many false positives (FPs).

Although the aforementioned dual-stage CAD systems demonstrated promising performance for lung nodule detection, these techniques are adds the computational complexity by increasing the number of DNNs to train. Also, such techniques are more prone to error, subsequently, limits the performance. Specifically, nodule those are missed at the first stage cannot be recoverable at the second stage of false positive reduction and sensitivity at detection stage is kept high which significant increases the FPs, results in increasing the load for the FPs reduction stage. To address this issue, many studies proposed single stage CADe system which perform the nodule detection and false positive reduction simultaneously by using the same network. For instance in [30] Li et. al., used the 3D Encoder-Decoder architecture for lung nodule detection. To effectively reduce the false positive, they utilize a dynamically scaled cross entropy loss. Similarly, in [31] Wu et. al., combined the image enhancement and a Dual-branch neural network for improving the visibility of lung nodules by suppressing the noises from background. The enhanced images were fed to the architecture which consists of two U-Nets to detect the nodules. In [32] Zhu et. al. utilized 3D residual U-Net with improved attention gate to reduce the false positives. They also applied channel interaction unit prior to the detection head and the gradient harmonizing mechanism loss function was used combat the problem of imbalance of positive and negative samples problem. In [33] Luo et. al. detected the position, radius, and offset of nodules by using an anchor-free 3D sphere representation-based center-points matching detection network. They used bounding sphere to represent nodules with the centroid, radius, and local offset in 3D space and sphere-based intersection over-union loss function was used to train their model. To improve the positive center-points selection and matching, An online hard example mining and re-focal loss was employed. Such techniques greatly reduces the computational complexities and easier to optimize, however, they suffers from lower performance which limits their clinical usage.

The most of the existing deep learning-based methods have shown promising performance for real-time clinical usages. However, only a few techniques have strived to following the clinical workflow used by radiologist. Radiologists first examine the maximum intensity projection (MIP) images of CT scan to roughly screen the nodule candidates and use the raw CT scan slices to finalize the decision. MIP is a technique to project 3D data with maximum intensities to the plan of projection. MIP helps to summarize the shape variations appearing along the z-axis which improves the visibility of lung nodule by distinguishing it from surrounding structures inside the lung. It can be taken in both directions (i.e., forward and backward), each highlights the structural variations occurring in each direction. A few studies have

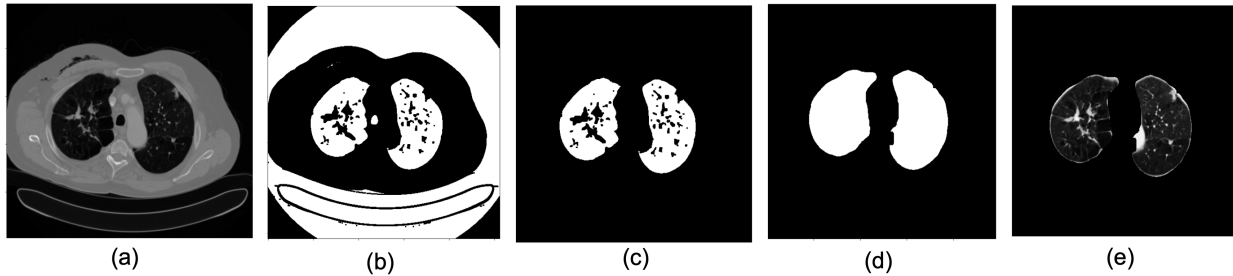


Fig. 1: The procedures of lung parenchyma segmentation. (a) A raw thoracic CT image; (b) the mask of air regions; (c) the mask after the removal of irrelevant objects other than lung region; (d) the dilated mask of lung parenchyma; (e) the image of segmented lung parenchyma.

also utilized the MIP images to improve the lung nodule detection performance. For instance, in [34] Masood et al. leveraged MIP to extract the meaningful insight of lung nodules from 3-D views (i.e., axial, coronal, and sagittal) and used multidimensional region-based fully convolutional network based CAD system for lung nodule detection and classification. They utilized multilayer fusion region proposal network in their architecture by using deconvolutional layer to improve the original RPN from faster R-CNN. Similarly, in [35] Zheng et. al. used MIP with different slab thickness (i.e., 5 mm, 10mm, 15mm) to train four U-Nets and merge their outputs for nodule candidates detection. Finally, for false positive reduction, they trained two different size DNNs which classified the candidate patch into nodule or non-nodule. Although, the leveraged MIP images to improve the nodule detection and strived to followed the clinical workflow, they trained four different networks and each network only relies on limited information (i.e., MIP images). In clinical practices, it is infeasible to utilize MIP images for diagnosis as it provides only limited information about the scan and even some cases, it suppress the nodules having lesser intensity values. Therefore, radiologist examines the raw CT scans complementary with MIP images of various thicknesses to draw the final conclusion about lung nodule. To incorporate this clinical workflow, we proposed Multi-Encoders based Deeply supervised network (MEDS-Net) based CAde system which incorporates the 3D patch of CT scan along with bi-directional MIP images of three different thicknesses (i.e., 3, 5 and 10mm) to detect the lung nodule. Most importantly, at the time of inference, we exploit the auxiliary outputs from various levels of decoder block to reduce the false positives. The results show that the propose CAde system is highly efficient and robust against various size and texture of the lung nodules.

II. MATERIALS

A. Datasets

The Lung Image Database Consortium and Image Database Resource Initiative(LIDC/IDRI) was an established repository of computed tomography scans to facilitate computer-aided systems on the assessment of lung nodule detection, classification and quantification. The LIDC/IDRI database consists of 1018 thoracic CT scans, acquired from 1010 different patients, with the corresponding nodule annotations. The process of annotating the nodules of the LIDC/IDRI database was

performed by four radiologists in two stages. In the first stage, each radiologist analyzed the exams individually. In the second stage, the results of the four analyses of the first stage were presented together to the four radiologists. During this stage, each of the radiologists re-analyzed the exams and again made their annotations independently. There were three nodule categorizations which were non-nodules, nodules with a size less than 3 mm in diameter and nodules with a size of equal to or larger than 3 mm in diameter. As nodules with diameter less than 3mm are labelled by only central points and easily corroded by image filters, it is inappropriate for this proposed method to detect small nodules. Therefore, the main task of this study is to automatically detect nodules with diameter greater than 3mm, which can be demonstrated in later sections. In addition, the nodules accepted by at least 3 out of 4 radiologists were used as the reference standard. In this way, 1186 valid nodules remained for the experiments.

III. PROPOSED METHODOLOGY

A. Data Preprocessing

1) *Lung Parcheyma Segmentation*: Since abdominal thoracic CT scan contains multiple organs (i.e., lung, liver, stomach, gall bladder, kidney etc.), we first devise a fully automatic scheme for lung parcheyma segmentation to isolate the volume of interest (VOI). The scheme consists of four steps which have been demonstrated in Fig. 1. Most of muscle, tissues, and bones in CT scans have Hounsfield values above -70 and air starts at -1000 [36]. At first, we created the air mask by binarizing the scan with threshold HU value of -800 as shown in Fig. 1(b). We pass the air mask to the watershed segmentation algorithm [37] to remove the irrelevant regions other than lung as shown in Fig. 1(c). To add the veins and nodules in the mask generated by watershed segmentation we apply dilation and erosion to masks Fig. 1(d). As the nodules and veins in the lung are mostly surrounded by air so dilating and eroding the air mask not only adds them but also smooths out the edges of the lung mask. This smoothing adds any nodule which is formed on the boundary of the lung as show in Fig. 1(e). After localizing the lung, we discarded all slices having no presence of lung.

2) *Scan Normalization*: Since the data set consists of scans having various slice thickness and pixel spacings, we first normalize the slice thickness and pixel spacing to 1mm. After normalizing the pixel spacing, we further to normalized the

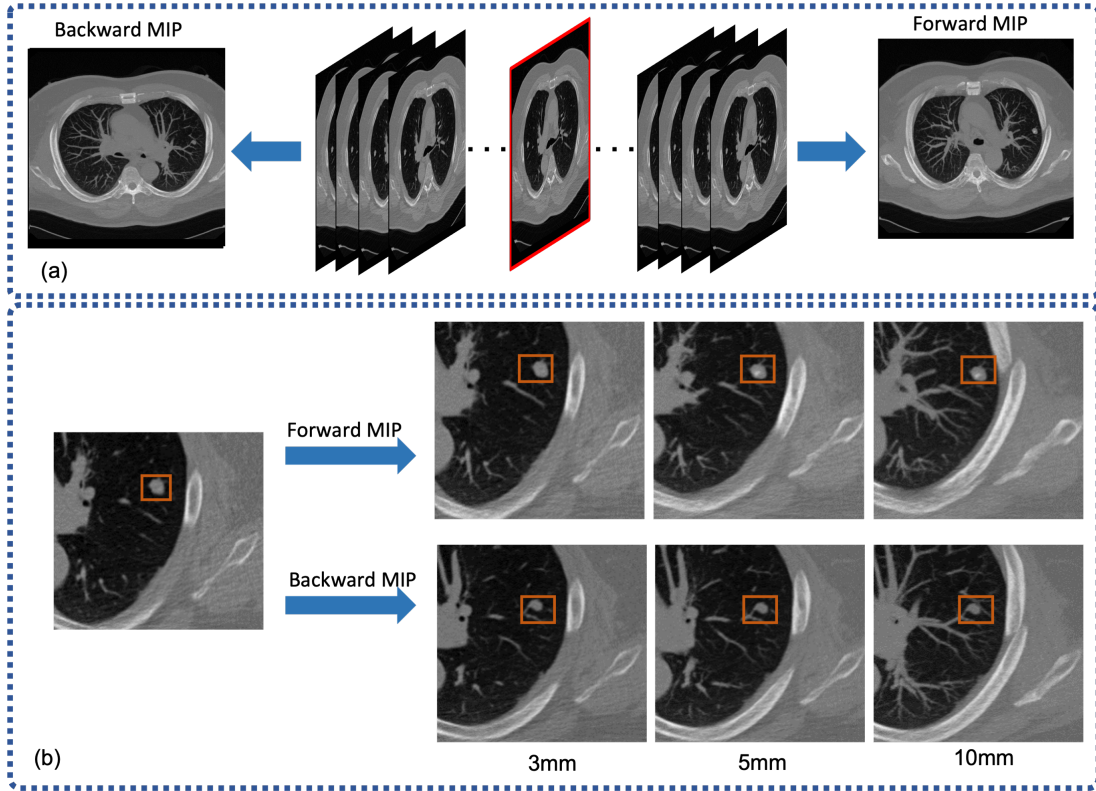


Fig. 2: a) Forward and Backward MIP b) Forward and Backward MIP of thickness 3mm, 5mm, 10mm (left to right)

spatial resolution by cropping the each slice equally from all sides to normalize the dimensions to 256×256 . Here we leveraged the lung masks to avoid the removal of lung region during the normalization. We also normalized the HU values to improve the contrast of lung region. Particularly, we set the window level from -1000 HU to 400 HU and normalize images to the range between 0 and 1 which is described in the equation (1).

$$\vec{F}(x, y) = \begin{cases} 0, & f(x, y) < -1000 \\ \frac{f(x, y) + 1000}{1400}, & -1000 \leq f(x, y) \leq 400 \\ 1, & f(x, y) > 400 \end{cases} \quad (1)$$

where $f(x, y)$ and $\vec{F}(x, y)$ are the original CT value and the transformed grayscale value, respectively.

Similarly, we normalize the slice thickness and pixel spacing of all the scans to 1mm and eventually, each slice is cropped from each side to normalize the dimensions to 256×256 .

B. Bi-Direction Maximum Intensity Projection

Maximum Intensity Projection (MIP) has proven extremely effective for lung nodule detection [1]. Subsequently, in clinical practice, radiologists examine the slices of raw thoracic CT complementing with MIP images of various slab thicknesses (i.e., 5mm and 10mm). The raw slices help to differentiate between suddenly appeared nodules and vessels, since nodules can be easily confused with vessels in a single slice. While, MIP images improve detection of pulmonary nodules, especially small nodules. MIP consists of projecting the voxel with the highest HU value on every view throughout the slab of certain

thickness onto a 2D image. Such a combined image shows morphological structures of isolated nodules and continuous vessels. Traditionally, MIP is taken into one direction along z-axis which helps to distinguish nodules from the vessels penetrating into one direction. To improve the visibility of nodules, in our work, we propose the bi-directional MIP images to improve the nodules visibility as shown in Fig 2. Particularly, we take the maximum intensities projections of certain slab thickness from both directions along z-axis as depicted in Fig. 2(a). We incorporated MIP images of three slab thicknesses, i.e., 3mm, 5mm and 10mm as these thicknesses have effective in clinical diagnosis of lung nodules [38]. The example of bi-directional MIP images of different thicknesses have been shown in Fig. 2(b). It can be noticed that forward and backward MIP images give different textural information that provides those details of the nodule which are occluded by vessels or lung tissues.

C. Self Distilled Multi-Encoders Network

The proposed MEDS-Net is an end-to-end lung nodule detection framework which is demonstrated in Fig. ?? and summarized as follows: (1) First 3D slab consisting of total 11 slices (i.e., 11) of 1mm thickness to dense-block which squeeze the representation into three channels by using Dense-block. (2) The compressed features along with forward and backward MIP images are inputted into encoders-block which contains three encoders to extract the meaningful features from each three channel input; (3) The extracted features at various levels of encoders are concatenated to combine with the corresponding decoder layers via residual connections to

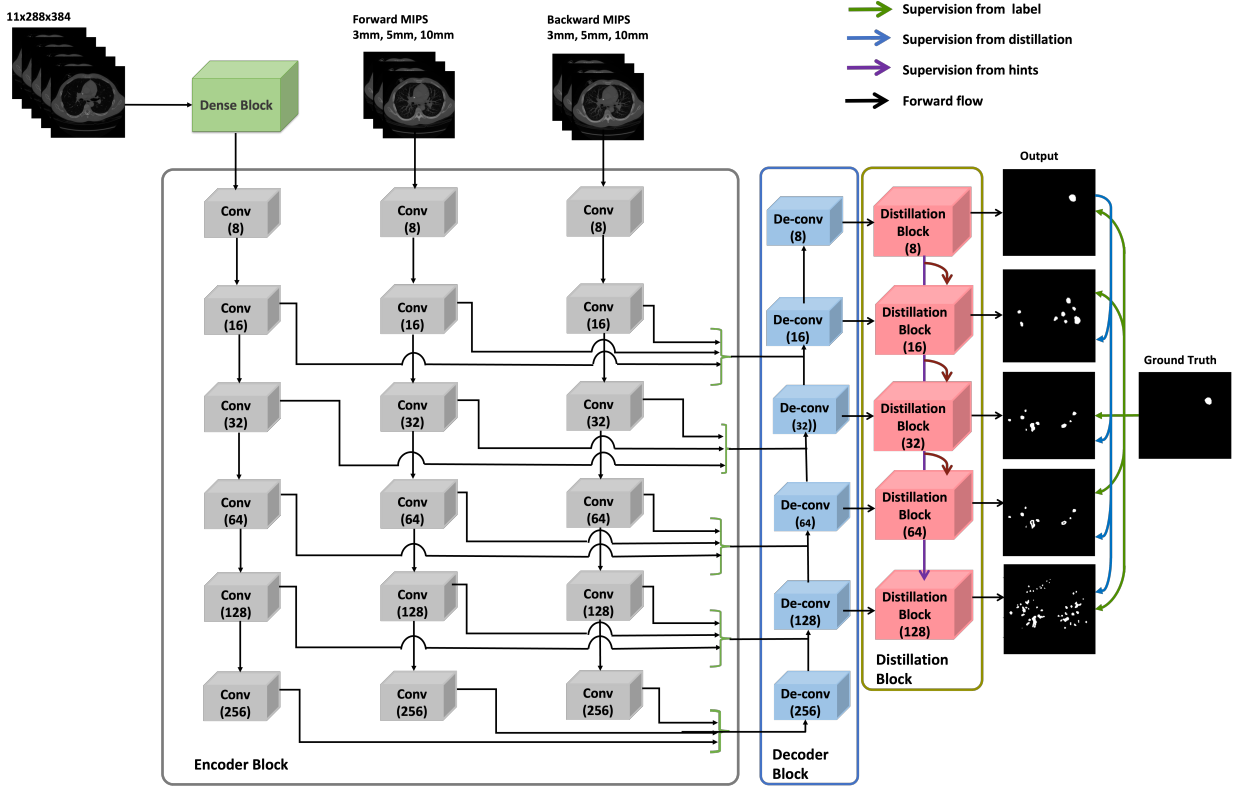


Fig. 3: Illustration of our proposed multi-Encoders network with self distillation.

decoder block; (4) Decoder-block utilizes the deconvolutional layers to up-sample the latent features at different stage and at various levels of decoder the features are reshapes the high-level features to the same size as the input image to acquire the segmentation result; (5) Finally, outputs at four different levels have been up-sampled by employing deconvolutional layers in deep supervision block.

1) *Dense-Block*: To incorporate the spatial sequential information which is crucial to detect the small nodules, we also input a patch of scan to the proposed architecture. Concretely, the five adjacent slices from both sides (i.e., forward and backward) of the central slice, i.e., 3D patch of depth $11 \times 256 \times 256$ from around the slice is extracted, and inputted into 3D Dense-Block. The 3D Dense-Block takes 11 slices of 1mm thickness as input and transforms into meaningful latent representative of same dimension as MIP images input, i.e., $3 \times 256 \times 256$. As shown in Fig. 4(a), the 3D dense block is composed of four sets of dense units followed by the maxpooling layers and in fifth dense unit is followed by the reshaping layer which squeezes the information to desired dimensions. Fig. 4 shows the architecture of each dense-unit which is composed of 5 sets of 3D convolution, Relu activation and batch normalization. Output of each set is propagated to every next set using skip connection. After each dense unit features are down-sampled along z-axis, subsequently, at the end of the dense block we have a 2D feature maps, consisting of three channels, from the 3D input patch. This feature map along with MIPs of input scan is passed to the encoders-block to further refine the features pertaining to the nodule detection.

2) *Encoder Block*: In Fig. 3, the overall structure of encoder-block has been demonstrated which includes three coding paths, namely, 3D patch, forward and backward MIPs encoders. All three encoders are kept identical and inspired by conventional UNet encoder [39]. Nevertheless, our encoders are more deeper than the standard UNet encoders to effectively learn the meaningful insights which are crucial to distinguish the lung nodule from complex anatomical structure of lung. Concretely, each encoder-branch consists of six Conv-Blocks which down-samples the input to lower dimensions while extracting the meaningful features. As shown in Fig. 5 (a), Conv-Block has been described, it contains two stages; the first stage has two 2D convolutional layers followed by a batch normalization layer, then a skip connection is used to combine the input with the output features of first the convolution stage. This type of short skip connections tend to stabilize gradient updates. At second stage, the combined features are inputted to same set of layers as first stage followed by an additional downsample layer. The width of each of our branches is kept small to avoid overfitting; our first conv-block contains 8 features maps, these get double after every downsampling layer and eventually, our final conv-block has 256 features. The output features of all three layers are then concatenated together at each resolution.

3) *Decoder Block*: The proposed architecture leverages rich information extracted from three types of inputs, i.e., forward, backward MIP and patch of 1mm CT slices, this information is extracted from encoders at multiple scales by adding the residual connections to decoder block. Fig. 3

describes the architecture of Decoder-Block which is fed with the outputs from all three encoders. Decoder-block consists of six DeConv-Blocks which up-samples the input features while extracting the useful information at different levels. Fig. 5 (b), describes the architecture of DeConv-Block which consists of two stages, in stage one two convolution blocks are followed by a batch normalisation layer. Output features of stage one are combined with input features using a skip connection and forwarded to stage two. The second stage is similar to the first one followed by upsampling layer. Decoder increases the dimension of features step by step till the final deconvolution block, which has the same feature dimension as the ground truth mask. Further, we have connected the distillation blocks at five stages of decoder. Main purpose of this block is to convert the features instantaneously to predicted output masks rather than going step by step from decoder layers.

D. Self Distillation

The proposed framework employs self-distillation mechanism to improve the training process. The decoder-block is divided into several shallow detector by using distillation block as shown in Fig. 3. Particularly, the deepest five DeConv-Blocks in the decoder-block are connected with distillation units. Each distillation unit is responsible of immediately up-scaling the features to generate the lung nodule mask. We call the deepest branch as main detector and intermediate branches as shallow detectors. Fig 5 (c) describes the architecture of distillation units. First layer of distillation unit is an up-sampling layer which directly up-scale the feature to lung nodule’s mask height and width. Second layer is a 2d convolution layer with relu activation and final layer is also a convolution layer of single filter and softmax activation. During the training process, all the shallow detectors are trained as student models via distillation from the deepest detector, which can be conceptually regarded as the teacher model. Similar to [40], to improve the learning ability of student detectors in proposed framework, we utilize three types of losses during the training processes:

LS1: It is the dice loss which is calculated with labels of training data to all the detector networks outputs. Here we provide equal opportunity to all the detector networks to learn from knowledge hidden in the dataset via labels. LS2: KL (Kullback-Leibler) divergence loss under teacher’s guidance. The KL divergence is computed using softmax outputs between students and teachers, and introduced to the softmax layer of each auxiliary detector network. By introducing KL divergence, the proposed framework distill the knowledge from the teacher’s networks, the deepest one and main network, to each student, intermediate auxiliary detector networks. LS3: It is L2 loss which is computed between the feature maps of main detector network and each auxiliary detectors.

E. False Positive Reduction using Shallow Detectors

In contrast to previous studies in which false positive reduction is performed by separate network, our framework exploits the outputs of the shallow detectors to reduce the false positive

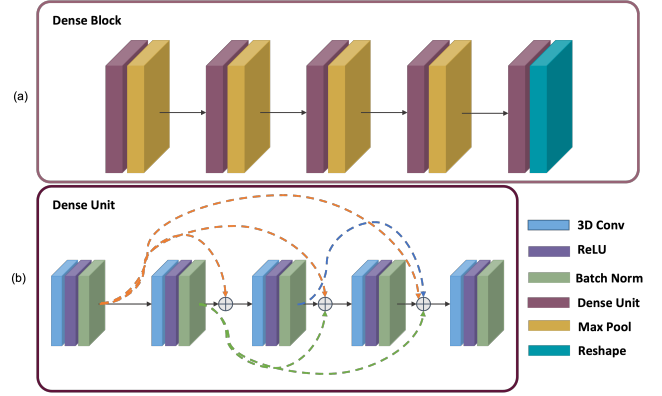


Fig. 4: Illustration of Dense Block.

at the time of inference. Concretely, all the nodules detected by the main detector are considered as nodule candidates and shallow detectors complement the detection of main detector to validate the candidates. A candidate is considered nodule only if at least two among four shallow detectors approve the decision of main detector. Most importantly, we apply extreme confidence threshing (ECT) based strategy to consider the vote of each shallow detector. Particularly, ECT only allows to vote only those shallow detector that high confidence against the region of nodule candidate. ECT can be formulated as:

$$\vec{M}(p) = \begin{cases} 0, & p < C_P - C_B/2 \\ p, & \|p - C_P\| \leq C_B/2, \\ 1, & p > C_P + C_B/2 \end{cases} \quad (2)$$

Where, p represent the condense of shallow detector against the region of nodule candidate, the value of p ranges from 0 to 1; 0 denotes the absence of nodule and 1 represents the presence of nodule. Here, we define the region of confusion by using confusion point, C_P , and confusion band width, C_B . In this study, the values of C_P and C_B is set for each shallow detector by analyzing the results on the validation set.

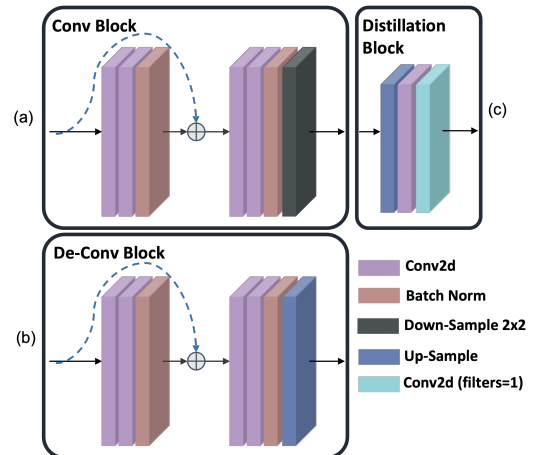


Fig. 5: Illustration of Convolutional and De-convolutional Blocks in (a) and (b), respectively.

F. Training Process

We divide the whole dataset into 10 subsets to perform 10-fold cross-validation. For each fold, 65%, 10% and 25% of the dataset has been used for training, validation and testing, respectively. The batch size is set to 3 due to the maximum memory of the GPU and the depth of CNNs. We have used adam optimizer with initial learning rate of 0.001 and first and second momentum of 0.9 for decay of learning rate. We use early stopping with a patience of 10 epochs to avoid overfitting. This study combination two losses, i.e., the dice score and binary cross entropy score coefficient, to calculate the loss value: To improve the performance and robustness of model, loss function is applied at three different stages of model.

First is Segmentation loss which is Dice loss of lung nodule mask with decoder output and every distillation block output. The dice loss is defined in (3), p_i is the i th voxel value of predicted mask and q_i is lung nodule mask i th voxel.

$$L_{Dice} = 1 - \frac{2 \sum_{i=1}^N p_i q_i}{\sum_{i=1}^N p_i^2 + \sum_{i=1}^N q_i^2} \quad (3)$$

Second loss is teacher student loss which also Dice loss between decoder's output and every distillation block output. Third loss is l2 loss between up-scaled feature of deepest distillation block and every other distillation block. l2 loss is defined in (4).

$$L_{l2} = \sum_{i=1}^N (p_i - q_i)^2 \quad (4)$$

IV. EXPERIMENTAL RESULTS AND DISCUSSION

A. Ablation Study

We start our evaluation by benchmarking the performance for Self-Distilled Multi-Encoders Network over its other variants. We analyze the effect input (i.e., 3D scan patch, forward and backward MIPs) to the encoders and self distillation, separately. The details of both analysis have been described in the following subsections.

B. Effect of Multi-Encoders

To analyze the effect of multi-encoders, we implemented single-encoder and dual-encoders versions of proposed architecture. Particularly, we implemented three single-encoder variants with 3D patch, forward and backward images input. Similarly, we implemented two dual-encoder variants, i.e., one with Bi-Directional MIP images input and other one is with 3D patch and forward MIP images. All the variants are implemented with self-distillation mechanism and followed by the same pipeline. To compare the performances of these variants models with proposed Multi-Encoders architecture for nodule detection, we analyze the FROC curves of each variant shown in Fig. 6. The single-encoder based architecture with 3D patch input has the lowest performance and it become worst when we tends to reduce the number of false positive per scan. Since only 3D patch of scan, consisting of 11 slices of 1mm thickness (i.e., of depth 10mm), is inputted to detect the

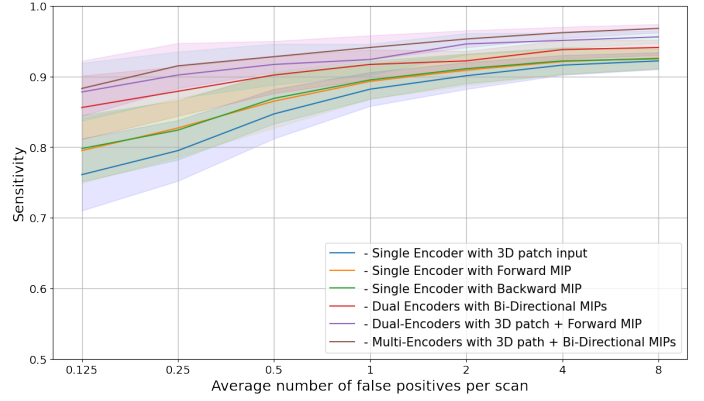


Fig. 6: FROC

nodule, network have limited information to detect the nodules which makes it challenging to detect nodules without false positives. Such as the nodule bigger than 10mm may appear like vessels and some small vessels may also appear similar to nodule which confuses the network and results into poor performance. On the other hand, the single-encoder versions with forward and backward MIP images demonstrate slightly better but similar performance due to the symmetrical effect of MIP images and conceptually, same amount of information was provided in both variants. It also shows that direction, (i.e., from top to bottom or bottom to top), of MIP images has no influence on the performance.

We also performed comparison with dual-encoders based architectures, for which make two combinations. At first, we utilized Bi-Directional, forward and backward, MIP images and achieved significantly improved performance which can be attributed to the fact that MIP images enhance the visibility of lung nodules, make it easier for network to distinguish them from other anatomical structure. Most importantly, Bi-Directional MIP images cover a reasonable depth of scan, i.e., 30mm, which enables the network better explore the insights of each suspected nodule region. However, MIP images have certain limitations while representing the information as they relies on maximum intensities which suppresses the information present in the intermediate intensities. Therefore, radiologists examines the nodules in the raw CT slices after initial screen in MIP images. To this end, we also implemented dual-encoders based variant with 3D patch and forward MIP images. The results demonstrate that the combination of raw slices of 1mm thickness with MIP images of various thickness are more effective than Bi-Directional MIPs as it equips the network with rich information which contains high level 3D aspect in the form of MIP as well as low level 2D slice level information which helps to distinguish and precisely locate the small nodules. Finally, combining raw patch of scan with Bi-Directional MIPs images in multi-Encoder architecture depicts the optimal and consistent performance for lung nodule detection.

C. Effect of Self Distillation

To analyze the effect of self distillation, we implemented the variant of proposed architecture without self distillation.

TABLE I: PERFORMANCE COMPARISON WITH OTHER COMPUTER-AIDED DETECTION SYSTEMS ON THE LUNA16 DATASET

Total number of scans: 888							
Total number of nodules: 1186 (3-10 mm: 905, 10-20 mm: 231, ≥ 20 mm: 50)							
Feature Level	Number of detected nodules (3-10mm)	Number of detected nodules (10-20mm)	Number of detected nodules (≥ 20 mm)	Total number of detected nodules	Sensitivity (%)	False Positives (FPs)	FPs per scan
Multi-Encoders Net (without Self-Distillation)	862	202	50	1114	93.93	28910	32.56
Detector 1/5	841	195	46	1082	91.23	30226	34.04
Detector 2/5	857	198	48	1103	93	26954	30.35
Detector 3/5	856	205	50	1111	93.68	22047	24.83
Detector 4/5	877	212	50	1139	96.04	19338	21.78
Detector 5/5	889	221	50	1160	97.81	18004	20.27
Ensemble	901	228	50	1179	99.41	36780	41.42

TABLE II: PERFORMANCE COMPARISON WITH OTHER COMPUTER-AIDED DETECTION SYSTEMS ON THE LUNA16 DATASET

CAD Systems	Sensitivity (%)	Total number of candidates	Average number of candidates per scan
Zheng et al. [35]	95.4	18,116	20.4
Setio et al. [41]	31.8	258,075	290.6
Yuan et al. [27]	94	44,627	50.25
Pereira et al. [28]	98.15	44,111	49.67
Wang et al. [42]	96.8	53,484	60.2
Zhang et al. [43]	100	45,939	51.7
Setio et al. [44]	98.3	754,975	850.2
Tarres et al. [45]	76.8	19,687	22.2
Our Method	97.8	19,190	21.61

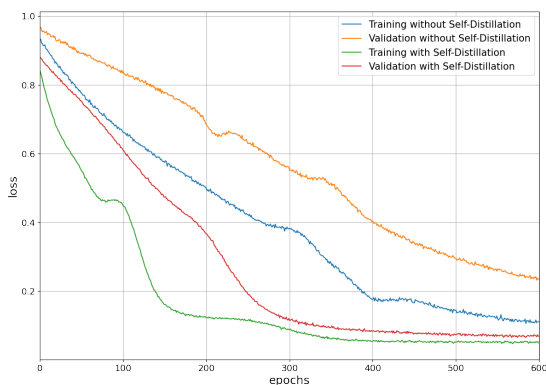


Fig. 7: The constant and adaptive region of interests (ROIs) have been shown in a sequence of slices in which nodule is present. Blue and red boxes represent the constant ROIs, while green boxes depict the adaptive ROI.

We analyzed the effect of self distillation during the training process and inference. Conceptually, self distillation is an extended version of deep supervision which is proven to be effective to address the vanishing gradient problem. Subsequently, self distillation mechanism in proposed framework assists the training process to optimize the network weights. The training and validation curves of both variants have been shown in Fig. 7. The results show that the introduction of self distillation scheme improves the convergence rate as well as helps to optimize the learning by achieving the lower training and validation losses. These improvements can be attributed to the supervision of the deeper layers at multiple levels which encourages the earlier layers to learn more meaningful and representative features for improved detection of lung nodules.

In addition, employment of self distillation greatly helps to expedite the network convergence by avoiding the issue of gradient vanishing [46] that are commonly faced while training deeper 3D CNNs.

We further analyze the performance of each detector in the proposed SDME-Net. Table II summarizes the results obtained from all the detectors including the baseline implementation of multi-Encoder architecture without self distillation. An ensemble result is obtained by simply including all the nodules candidates detected by each detector. The results demonstrate that (i) all the networks have acquired significant performance improvement by exploiting self distillation mechanism. (ii) The proposed SDME-Net has overall effectively detected almost all the nodules, achieved the sensitivity 99.41%, with its five detectors. Most importantly, the total number of nodules detected by the ensemble scheme is not equal to the total nodules detected by each detector. This means that each detector detected nodule independently (iii) The overall performance of deeper detectors is improved; however, a number of nodules missed by deeper networks have been detected by less deep network, indicating that each detector has detected nodule independently. (iv) The self distillation plays a crucial role in the improvement of the deepest network, main detector. The introduction of four shallow detectors improves 4.08% sensitivity of main detector and significantly reduced the number of false positives per scan.

D. Comparison with the previous studies

Typical CAD systems consist of two stages, i.e., candidate detection and false positive reduction, and mostly two separate networks are trained to achieve this goal. Nevertheless, in this study, the proposed framework combines both stages by employing self distillation. All the nodules detected by the main, deepest detector, are considered as nodule candidates and the capability of nodule detection of the proposed framework has been compared with the recently published individual candidate detection systems. Table III summarizes the results of candidate detection stages of recently published works. Setio et al. [41] and Tarres et al. [45], employed classical algorithms based on machine learning while Zheng et al. [35], Yuan et al. [27], Pereira et al. [28], Wang et al. [42], Setio et al. [44] and our proposed framework utilize the deep learning based methods. Zhang et al. [43] developed a hybrid method by combining classical techniques with advanced deep learning based algorithms.

TABLE III: PERFORMANCE COMPARISON WITH OTHER COMPUTER-AIDED DETECTION SYSTEMS ON THE LUNA16 DATASET

CAD System	Year	Type of scheme	False positive per scan							CPM
			0.125	0.25	0.5	1	2	4	8	
Setio et al. [44]	2017	Dual-stage	0.859	0.937	0.958	0.969	0.976	0.982	0.982	0.952
Wang et al. [42]	2018	Dual-stage	0.788	0.847	0.895	0.934	0.952	0.959	0.963	0.903
Zhang et al. [43]	2018	Dual-stage	0.89	0.931	0.944	0.949	0.965	0.972	0.976	0.947
Zheng et al. [35]	2019	Dual-stage	0.876	0.899	0.912	0.927	0.942	0.948	0.953	0.922
Cao et al. [22]	2020	Dual-stage	0.848	0.899	0.925	0.936	0.949	0.957	0.96	0.925
Li et al. [30]	2020	Single-stage	0.6	0.674	0.751	0.824	0.85	0.853	0.859	0.773
Zhou et al. [26]	2022	Dual-stage	0.742	0.84	0.8989	0.925	0.944	0.954	0.959	0.895
Zhao et al. [24]	2022	Dual-stage	0.656	0.754	0.833	0.917	0.951	0.97	0.977	0.865
Agnes et al. [47]	2022	Dual-stage	0.803	0.89	0.93	0.959	0.967	0.979	0.981	0.93
Zhu et al. [32]	2022	Single-stage	0.782	0.834	0.893	0.917	0.932	0.952	0.956	0.895
Mei et al. [29]	2022	Dual-stage	0.712	0.802	0.865	0.901	0.937	0.946	0.955	0.874
Guo et al. [48]	2022	Single-stage	0.832	0.886	0.928	0.937	0.946	0.952	0.959	0.92
Our Framework	2022	Single-stage	0.883	0.915	0.928	0.941	0.953	0.962	0.968	0.936

Overall the performance of deep learning based methods is better than the conventional algorithms. Zhang et al. [43], Setio et al. [41] and Pereira et al. [28] achieved better detection rate. However, these studies had improved the true positives at the cost of several-folds higher number of FPs. Similar to our work, Zheng et al. [35] exploited the MIP images of various thickness to achieved 95% sensitivity with 20.1 candidates per scan. This shows the effectiveness of MIP image for lung nodule detection. Although Zheng *et al.* [35] trained four individual 2D networks with uni-directional MIP images, our framework consisting of single network outperforms in term of sensitivity by exploiting Bi-Directional MIP images. The results demonstrate that incorporation of Bi-Directional MIP images in network with self distillation significantly improves the nodule detection capability of proposed architecture.

To provide a comparative analysis and show the generality of these systems, we chose the published approaches which used the CPM for evaluation on the LUNA16 dataset. Table III summarizes the performance of these techniques. Among all the listed method, Setio et al. [44] demonstrated the best performance which is attributed to the combination of seven different nodule detection systems and five false positive reduction systems with varied architectures to detect the different type of nodules, such as subsolid, juxta-vascular, juxta-pleural nodules, etc. Nevertheless, the proposed scheme is designed for all the types of nodules and consisting on a single architecture. Our scheme exhibits comparable performance, even significantly better sensitivity for the small value of FPs per scan (i.e., 0.125). Similarly, Zhang et al. [43] achieved better performance by maintaining 100% sensitivity at the candidate detection stage with multi-scale LoG filters which cost more FPs compared to our scheme. Our scheme exploits Bi-Directional MIPs with different levels of thickness to achieve comparable results. For the smaller value of FPs per scan, our sensitivity is only 0.7% lesser which evident the effectiveness of self distillation strategy to optimize the performance. Although Agnes et al. [47] has lower CPM score, their sensitivities are higher when the false positive rate is bigger than one. A possible explanation for this they had utilized two stage scheme in which they first exploit UNet+ architecture of nodule detection and employed LSTM

based architecture for false positive reduction which makes the technique more complex. Similarly Cao et al. [22] has shown better performance for larger values of false positive rate by using two stage strategy. Guo et al. [48] has obtain lesser CPM and its performance degrades for smaller value of false positives. Similarly, Li et al. [30], Zhao et al. [24], and Mei et al. [29] obtained lower performance than the proposed scheme. Most importantly, our CADE system significantly outperforms single stage systems.

[49]

V. CONCLUSION

This work propose a novel self distillation based multi-encoders network which leverages Bi-Directional maximum intensity projection (MIP) images of various depths for lung nodule detection CAD system. Particularly, along with 3D patch of scan, proposed framework utilizes forward and backward MIP images of 3, 5 and 10mm thickness as input improve the networks learning. The study design multi-encoders architecture to incorporate these inputs and to improve the learning process of network self distillation has been employed at the decoder block. Most importantly, unlike conventional CAD system, the study exploits the auxiliary detectors to reduce the false positives which avoids the extra computational costs caused by the separate false positive reduction networks. The framework has been verified and evaluated on the widely used LUNA16 public dataset, and ablation experiments are conducted to demonstrate the importance of each component. The results show that employment of self distillation significantly improve the learning process by supervising the intermediate layers of decoder block. MEDS-Net exploits multi-scale features learning by using intermediate auxiliary outputs branches originating from various levels of decoder block to minimize the false positives. The proposed MEDS-Net is The results show that this network has excellent detection performance for the diversity and morphology of nodules and has the ability to accurately distinguish false-positive nodules. The CPM scores of the proposed method can be as high as 0.936, superior to the most advanced competitive networks.

REFERENCES

- [1] H. Sung, J. Ferlay, R. L. Siegel, M. Laversanne, I. Soerjomataram, A. Jemal, and F. Bray, "Global cancer statistics 2020: Globocan estimates of incidence and mortality worldwide for 36 cancers in 185 countries," *CA: A Cancer Journal for Clinicians*, vol. 71, no. 3, pp. 209–249, 2021. [Online]. Available: <https://acsjournals.onlinelibrary.wiley.com/doi/abs/10.3322/caac.21660>
- [2] G. D. Rubin, "Lung nodule and cancer detection in ct screening," *Journal of thoracic imaging*, vol. 30, no. 2, p. 130, 2015.
- [3] H. Y. Jiang, H. Ma, W. Qian, and G. H. Wei, "Risk analysis for pathological changes in pulmonary parenchyma based on lung computed tomography images," *Journal of computer assisted tomography*, vol. 40, no. 3, pp. 357–363, 2016.
- [4] G. D. Rubin, J. K. Lyo, D. S. Paik, A. J. Sherbondy, L. C. Chow, A. N. Leung, R. Mindelzun, P. K. Schraedley-Desmond, S. E. Zinck, D. P. Naidich *et al.*, "Pulmonary nodules on multi-detector row ct scans: performance comparison of radiologists and computer-aided detection," *Radiology*, vol. 234, no. 1, pp. 274–283, 2005.
- [5] Y. Gu, J. Chi, J. Liu, L. Yang, B. Zhang, D. Yu, Y. Zhao, and X. Lu, "A survey of computer-aided diagnosis of lung nodules from ct scans using deep learning," *Computers in Biology and Medicine*, vol. 137, p. 104806, 2021.
- [6] W. Cao, R. Wu, G. Cao, and Z. He, "A comprehensive review of computer-aided diagnosis of pulmonary nodules based on computed tomography scans," *IEEE Access*, vol. 8, pp. 154007–154023, 2020.
- [7] B. Liu, W. Chi, X. Li, P. Li, W. Liang, H. Liu, W. Wang, and J. He, "Evolving the pulmonary nodules diagnosis from classical approaches to deep learning-aided decision support: three decades' development course and future prospect," *Journal of cancer research and clinical oncology*, vol. 146, no. 1, pp. 153–185, 2020.
- [8] A. A. Rezaie and A. Habiboghli, "Detection of lung nodules on medical images by the use of fractal segmentation," 2017.
- [9] B. Wang, X. Tian, Q. Wang, Y. Yang, H. Xie, S. Zhang, and L. Gu, "Pulmonary nodule detection in ct images based on shape constraint cv model," *Medical physics*, vol. 42, no. 3, pp. 1241–1254, 2015.
- [10] Z. Ge, B. Sahiner, H.-P. Chan, L. M. Hadjiiski, P. N. Cascade, N. Bogot, E. A. Kazerooni, J. Wei, and C. Zhou, "Computer-aided detection of lung nodules: false positive reduction using a 3d gradient field method and 3d ellipsoid fitting," *Medical physics*, vol. 32, no. 8, pp. 2443–2454, 2005.
- [11] W. Guo and Q. Li, "High performance lung nodule detection schemes in ct using local and global information," *Medical Physics*, vol. 39, no. 8, pp. 5157–5168, 2012.
- [12] S. A. El-Regaily, M. A. M. Salem, M. H. A. Aziz, and M. I. Roushdy, "Multi-view convolutional neural network for lung nodule false positive reduction," *Expert systems with applications*, vol. 162, p. 113017, 2020.
- [13] D. P. Agrawal, B. B. Gupta, H. Wang, X. Chang, S. Yamaguchi, and G. M. Pérez, "Guest editorial deep learning models for industry informatics," *IEEE Transactions on Industrial Informatics*, vol. 14, no. 7, pp. 3166–3169, 2018.
- [14] M. S. Hossain, M. Al-Hammadi, and G. Muhammad, "Automatic fruit classification using deep learning for industrial applications," *IEEE Transactions on Industrial Informatics*, vol. 15, no. 2, pp. 1027–1034, 2018.
- [15] Z. Shi, L. Zhang, Y. Sun, and Y. Ye, "Multiscale multitask deep netvlad for crowd counting," *IEEE Transactions on Industrial Informatics*, vol. 14, no. 11, pp. 4953–4962, 2018.
- [16] M. Alencastre-Miranda, R. M. Johnson, and H. I. Krebs, "Convolutional neural networks and transfer learning for quality inspection of different sugarcane varieties," *IEEE Transactions on Industrial Informatics*, vol. 17, no. 2, pp. 787–794, 2020.
- [17] Z. Liu, Z. Wu, T. Li, J. Li, and C. Shen, "Gmm and cnn hybrid method for short utterance speaker recognition," *IEEE Transactions on Industrial Informatics*, vol. 14, no. 7, pp. 3244–3252, 2018.
- [18] M. Usman, B.-D. Lee, S.-S. Byon, S.-H. Kim, B.-i. Lee, and Y.-G. Shin, "Volumetric lung nodule segmentation using adaptive roi with multi-view residual learning," *Scientific Reports*, vol. 10, no. 1, pp. 1–15, 2020.
- [19] M. S. Lee, Y. S. Kim, M. Kim, M. Usman, S. S. Byon, S. H. Kim, B. I. Lee, and B.-D. Lee, "Evaluation of the feasibility of explainable computer-aided detection of cardiomegaly on chest radiographs using deep learning," *Scientific Reports*, vol. 11, no. 1, pp. 1–11, 2021.
- [20] Z. Ullah, M. Usman, M. Jeon, and J. Gwak, "Cascade multiscale residual attention cnns with adaptive roi for automatic brain tumor segmentation," *Information Sciences*, vol. 608, pp. 1541–1556, 2022.
- [21] A. Rehman, M. Usman, R. Jawaid, S. S. Byon, S. H. Kim, B. D. Lee, Y. G. Shin *et al.*, "Dual-stage deeply supervised attention-based convolutional neural networks for mandibular canal segmentation in cbct scans," *arXiv preprint arXiv:2210.03739*, 2022.
- [22] H. Cao, H. Liu, E. Song, G. Ma, X. Xu, R. Jin, T. Liu, and C.-C. Hung, "A two-stage convolutional neural networks for lung nodule detection," *IEEE journal of biomedical and health informatics*, vol. 24, no. 7, pp. 2006–2015, 2020.
- [23] A. Pezeshk, S. Hamidian, N. Petrick, and B. Sahiner, "3-d convolutional neural networks for automatic detection of pulmonary nodules in chest ct," *IEEE journal of biomedical and health informatics*, vol. 23, no. 5, pp. 2080–2090, 2018.
- [24] D. Zhao, Y. Liu, H. Yin, and Z. Wang, "An attentive and adaptive 3d cnn for automatic pulmonary nodule detection in ct image," *Expert Systems with Applications*, p. 118672, 2022.
- [25] H. Xie, D. Yang, N. Sun, Z. Chen, and Y. Zhang, "Automated pulmonary nodule detection in ct images using deep convolutional neural networks," *Pattern Recognition*, vol. 85, pp. 109–119, 2019.
- [26] Z. Zhou, F. Gou, Y. Tan, and J. Wu, "A cascaded multi-stage framework for automatic detection and segmentation of pulmonary nodules in developing countries," *IEEE Journal of Biomedical and Health Informatics*, 2022.
- [27] H. Yuan, Y. Wu, J. Cheng, Z. Fan, and Z. Zeng, "Pulmonary nodule detection using 3-d residual u-net oriented context-guided attention and multi-branch classification network," *Ieee Access*, vol. 10, pp. 82–98, 2021.
- [28] F. R. Pereira, J. M. C. De Andrade, D. L. Escuissato, and L. F. De Oliveira, "Classifier ensemble based on computed tomography attenuation patterns for computer-aided detection system," *IEEE Access*, vol. 9, pp. 123134–123145, 2021.
- [29] J. Mei, M.-M. Cheng, G. Xu, L.-R. Wan, and H. Zhang, "Sanet: A slice-aware network for pulmonary nodule detection," *IEEE transactions on pattern analysis and machine intelligence*, 2021.
- [30] Y. Li and Y. Fan, "Deepseed: 3d squeeze-and-excitation encoder-decoder convolutional neural networks for pulmonary nodule detection," in *2020 IEEE 17th International Symposium on Biomedical Imaging (ISBI)*. IEEE, 2020, pp. 1866–1869.
- [31] Z. Wu, Q. Zhou, and F. Wang, "Coarse-to-fine lung nodule segmentation in ct images with image enhancement and dual-branch network," *IEEE Access*, vol. 9, pp. 7255–7262, 2021.
- [32] X. Zhu, X. Wang, Y. Shi, S. Ren, and W. Wang, "Channel-wise attention mechanism in the 3d convolutional network for lung nodule detection," *Electronics*, vol. 11, no. 10, p. 1600, 2022.
- [33] Z. Wu, Q. Zhou, and F. Wang, "Coarse-to-fine lung nodule segmentation in ct images with image enhancement and dual-branch network," *IEEE Access*, vol. 9, pp. 7255–7262, 2021.
- [34] A. Masood, B. Sheng, P. Yang, P. Li, H. Li, J. Kim, and D. D. Feng, "Automated decision support system for lung cancer detection and classification via enhanced rfcn with multilayer fusion rpn," *IEEE Transactions on Industrial Informatics*, vol. 16, no. 12, pp. 7791–7801, 2020.
- [35] S. Zheng, J. Guo, X. Cui, R. N. Veldhuis, M. Oudkerk, and P. M. Van Ooijen, "Automatic pulmonary nodule detection in ct scans using convolutional neural networks based on maximum intensity projection," *IEEE transactions on medical imaging*, vol. 39, no. 3, pp. 797–805, 2019.
- [36] R. Bibb, D. Eggbeer, and A. Paterson, "2 - medical imaging," in *Medical Modelling (Second Edition)*, second edition ed., R. Bibb, D. Eggbeer, and A. Paterson, Eds. Oxford: Woodhead Publishing, 2015, pp. 7–34. [Online]. Available: <https://www.sciencedirect.com/science/article/pii/B9781782423003000020>
- [37] J. Angulo and D. Jeulin, "Stochastic watershed segmentation," in *ISMM (1)*, 2007, pp. 265–276.
- [38] R. Valencia, T. Denecke, L. Lehmkuhl, F. Fischbach, R. Felix, and F. Knollmann, "Value of axial and coronal maximum intensity projection (mip) images in the detection of pulmonary nodules by multislice spiral ct: comparison with axial 1-mm and 5-mm slices," *European radiology*, vol. 16, no. 2, pp. 325–332, 2006.
- [39] O. Ronneberger, P. Fischer, and T. Brox, "U-net: Convolutional networks for biomedical image segmentation," in *International Conference on Medical image computing and computer-assisted intervention*. Springer, 2015, pp. 234–241.
- [40] L. Zhang, J. Song, A. Gao, J. Chen, C. Bao, and K. Ma, "Be your own teacher: Improve the performance of convolutional neural networks via self distillation," in *Proceedings of the IEEE/CVF International Conference on Computer Vision*, 2019, pp. 3713–3722.

- [41] A. A. Setio, C. Jacobs, J. Gelderblom, and B. van Ginneken, "Automatic detection of large pulmonary solid nodules in thoracic ct images," *Medical physics*, vol. 42, no. 10, pp. 5642–5653, 2015.
- [42] J. Wang, J. Wang, Y. Wen, H. Lu, T. Niu, J. Pan, and D. Qian, "Pulmonary nodule detection in volumetric chest ct scans using cnns-based nodule-size-adaptive detection and classification," *IEEE access*, vol. 7, pp. 46 033–46 044, 2019.
- [43] J. Zhang, Y. Xia, H. Zeng, and Y. Zhang, "Nodule: Combining constrained multi-scale log filters with densely dilated 3d deep convolutional neural network for pulmonary nodule detection," *Neurocomputing*, vol. 317, pp. 159–167, 2018.
- [44] A. A. A. Setio, A. Traverso, T. De Bel, M. S. Berens, C. Van Den Bogaard, P. Cerello, H. Chen, Q. Dou, M. E. Fantacci, B. Geurts *et al.*, "Validation, comparison, and combination of algorithms for automatic detection of pulmonary nodules in computed tomography images: the luna16 challenge," *Medical image analysis*, vol. 42, pp. 1–13, 2017.
- [45] E. Lopez Torres, E. Fiorina, F. Pennazio, C. Peroni, M. Saletta, N. Camarlinghi, M. E. Fantacci, and P. Cerello, "Large scale validation of the m5l lung cad on heterogeneous ct datasets," *Medical physics*, vol. 42, no. 4, pp. 1477–1489, 2015.
- [46] X. Glorot and Y. Bengio, "Understanding the difficulty of training deep feedforward neural networks," in *Proceedings of the thirteenth international conference on artificial intelligence and statistics. JMLR Workshop and Conference Proceedings*, 2010, pp. 249–256.
- [47] S. A. Agnes, J. Anitha, and A. A. Solomon, "Two-stage lung nodule detection framework using enhanced unet and convolutional lstm networks in ct images," *Computers in Biology and Medicine*, vol. 149, p. 106059, 2022.
- [48] Z. Guo, L. Zhao, J. Yuan, and H. Yu, "Msanet: Multiscale aggregation network integrating spatial and channel information for lung nodule detection," *IEEE Journal of Biomedical and Health Informatics*, vol. 26, no. 6, pp. 2547–2558, 2021.
- [49] A. A. A. Setio, F. Ciompi, G. Litjens, P. Gerke, C. Jacobs, S. J. Van Riel, M. M. W. Wille, M. Naqibullah, C. I. Sánchez, and B. Van Ginneken, "Pulmonary nodule detection in ct images: false positive reduction using multi-view convolutional networks," *IEEE transactions on medical imaging*, vol. 35, no. 5, pp. 1160–1169, 2016.